Theor Chem Acc (2014) 133:1411
DOI 10.1007/s00214-013-1411-3

REGULAR ARTICLE

Intramolecular charge transfer and sensing mechanism for a colorimetric fluoride sensor based on 1,8-naphthalimide derivatives

Jun-Sheng Chen · Run-Ze Liu · Yang Yang · Tian-Shu Chu

Received: 1 August 2013 / Accepted: 17 October 2013 / Published online: 17 November 2013

Abstract The sensing mechanism of a fluoride colorimetric chemosensor 4-(*tert*-butyldimethylsilyloxy)-*N*-butyl-naphthalimide has been studied with density functional theory and time-dependent density functional theory methods. The theoretical results suggest that the low barrier of the desilylation reaction is responsible for the rapid response speed to the fluoride anion of the chemosensor. The calculated vertical excitation energies in the ground state of the chemosensor and its desilylation product agree well with the experimental UV–Vis absorbance spectra. It is also found that the intramolecular charge transfer process of the first excited state of the desilylation product induces the redshift of the absorbance and fluorescence spectra of the desilylation product compared with that of the chemosensor. Further, the previously experimentally incorrect assignment of the ^{1}H NMR spectrum of the desilylation product has been rectified in the present theoretical study.

Electronic supplementary material The online version of this article (doi:10.1007/s00214-013-1411-3) contains supplementary material, which is available to authorized users.

J.-S. Chen · R.-Z. Liu · Y. Yang · T.-S. Chu (✉)
State Key Laboratory of Molecular Reaction Dynamics, Dalian Institute of Chemical Physics, Chinese Academy of Sciences, Dalian 116023, People's Republic of China
e-mail: tschu@dicp.ac.cn; tschu008@163.com

J.-S. Chen · R.-Z. Liu
University of the Chinese Academy of Sciences, Beijing 100049, People's Republic of China

T.-S. Chu
Laboratory of New Fiber and Modern Textile, The Growing Base for State Key Laboratory, Institute for Computational Sciences and Engineering, Qingdao University, Qingdao 266071, People's Republic of China

Keywords Colorimetric sensor · Sensing mechanism · Density functional calculations · Desilylation reaction · Intramolecular charge transfer (ICT) · Naphthalimide

1 Introduction

In recent years, a number of chemosensors for fluoride anion have been developed [1–7] due to the considerable significant role of fluoride to health, environment and industrial processes [8–10]. Among these chemosensors, ratiometric chemosensors with intrinsic advantages of taking the intensity ratio at two different absorption or emission wavelengths [6] can circumvent the effects of various interference factors, such as polarity, probe molecule concentration, photo-illumination and the microenvironment around the probe molecule [11]. Up to now, a plenty of ratiometric chemosensors for fluoride anion have been developed with supposed sensing mechanisms.

Fluoride anion owns unique physical and chemical properties that make it the most electronegative anion, the strong hydrogen-bond acceptor and the anion with a high affinity to silicon and boron. There are a series of ratiometric chemosensors for fluoride anion having been developed with the strategy that involves the hydrogen-bonding interactions [12–14], the Lewis acid/base interactions [13, 15, 16] and the fluoride-triggered Si(B, C)–O cleavage reactions [1–3, 6, 17, 18]. Among these chemosensors, those with *tert*-butyldimethylsilyl and *tert*-butyldiphenylsilyl belong to the reaction-based type [2] and exhibit higher selectivity and stability. The good ratiometric response of this sort of chemosensor can be ascribed to the fluoride-triggered Si–O cleavage reaction and intramolecular charge transfer (ICT) [1–3, 18, 19] or the

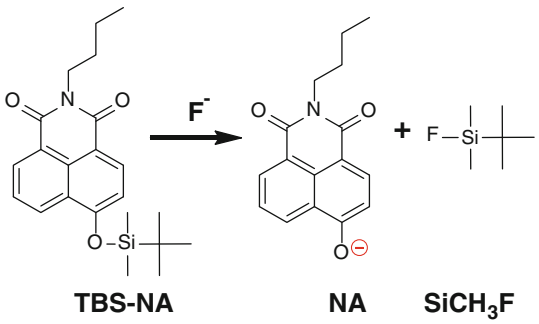

Scheme 1 Structures of **TBS-NA**, **NA** and **$SiCH_3F$**

excited-state proton transfer (ESPT) [20] or the excimer/monomer formation [6]. The photophysical properties and geometries of these chemosensors can be inferred from the measured ^{1}H NMR spectra, time-resolved absorption spectra and fluorescence spectra in the study of the Si–O bond cleavage, ICT and ESPT processes [2, 13]. As a complement to the experimental techniques, the density functional theory (DFT)/time-dependent functional theory (TD-DFT) methods are also suitable for studying the ICT, ESPT and photoinduced electron transfer processes by presenting direct and detailed information on geometries and other properties of chemosensors [16, 21–26].

Recently, a desilylation-reaction-based colorimetric chemosensor for fluoride anion, 4-(*tert*-butyldimethylsilyloxy)-*N*-butyl-naphthalimide (**TBS-NA**), has been reported by Ren and coworkers [27] (see Scheme 1). Like many previously reported ratiometric fluorescent chemosensors based on the fluoride-triggered Si–O cleavage reaction [2, 3, 6, 18, 20], the chemosensor **TBS-NA** also has the potential as a ratiometric fluorescent chemosensor. In order to understand the sensing mechanism of **TBS-NA** in detail, we carried out the DFT/TD-DFT calculations in the present study to investigate the ground- and the excited-state properties. The ^{1}H NMR spectra of **TBS-NA** and its desilylation product anion form **NA** have been calculated. The frontier molecular orbitals, electronic transition energies and corresponding oscillator strengths have been analyzed for both **TBS-NA** and **NA**. These theoretical results not only provide insight into the role played by the desilylation reaction and the ICT process in the sensing mechanism of **TBS-NA**, but also explained why **TBS-NA** can serve as a good ratiometric fluorescent chemosensor.

2 Theoretical methods

In this contribution, the electronic structure calculations for both the ground state and the excited state have been performed by using DFT/TD-DFT methods with Gaussian 09 program [28]. The B3LYP functional and the TZVP basis set, an appropriate basis set for the present ionic organic compound [22], have also been adopted in the calculation. Furthermore, a test of basis set adequacy was performed in our present work, showing that the calculation results obtained with TZVP basis set are nearly the same as the actual experimental ones and such calculation is not time-consuming (see Table S1). All electronic structure calculations were completed without constraint. All the local minima were confirmed by the vibrational frequencies analysis calculations at the optimized structures. In all electronic structure calculations, solvent effect was included using the integral equation formalism (IEF) version of polarizable continuum model (PCM) with the dielectric constant of acetonitrile (MeCN, $\varepsilon = 35.69$). Six electronic states were included in the present TD-DFT calculations. In order to obtain accurate spectral results and to reproduce the experimental conditions (i.e., the ^{1}H NMR spectra of **TBS-NA** and **NA** were conducted in chloroform, and other experimental spectra were conducted in MeCN), the gauge-independent atomic orbital method with high-level B3LYP/QZVP and IEF–PCM solvation model (chloroform, $\varepsilon = 4.71$) were employed to compute the ^{1}H NMR spectra of **TBS-NA** and **NA**. For the calculation of the potential energy surface of the desilylation process, all stationary points along the reaction coordinate were fully optimized with IEF–PCM (MeCN, $\varepsilon = 35.69$) DFT/B3LYP/TZVP method. Vibrational frequencies were analyzed at the optimized structures to obtain the thermodynamic corrections and confirm that these structures corresponded to the local minima or transition state. In order to confirm that the transition state connects the intermediate and products, the intrinsic reaction coordinate (IRC) calculations have been performed. All energies reported (ΔG_{MeCN}) were relative energies to corresponding energy of the reagents, with Gibbs free energy correction.

3 Results and discussion

3.1 Optimized ground-state structures

The ground-state geometries of the chemosensor **TBS-NA**, the fluoride complex form **TBS-NAF** and the anion product form **NA** were optimized at the B3LYP/TZVP level with an IEF–PCM solvation model (MeCN, $\varepsilon = 35.69$), and the optimized structures are displayed in Fig. 1. The atomic coordinates of these structures are provided in the Supporting Information. In Fig. 1, the calculated Si–O bond length is 1.72 Å in **TBS-NA**. With the addition of the fluoride anion, the Si–O bond is broken and a new F–Si bond is formed, which is verified by that the calculated distance of Si–O is 5.05 Å and the F–Si bond distance is 1.67 Å in **TBS-NAF** [29].

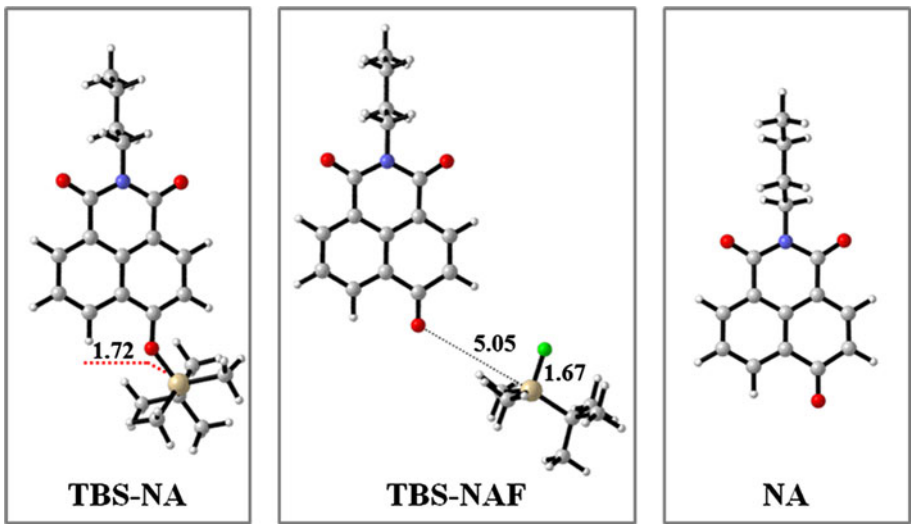

Fig. 1 Views of the optimized S_0 structures for **TBS-NA**, **TBS-NAF** and **NA** using B3LYP/TZVP, *gray*: C; *white*: H; *red*: O; *blue*: N; *green*: F; *yellowish brown*: Si

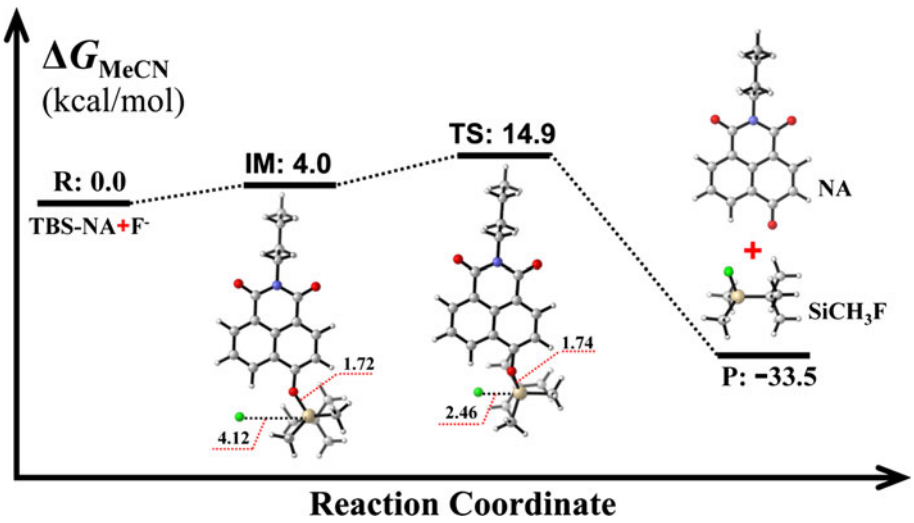

Fig. 2 Free energy profiles for the desilylation reaction mechanism. *R* reactant, *IM* intermediate, *TS* transition state, *P* product. All free energies are in kcal/mol; all bond lengths are in Å

To further elucidate the role of the fluoride-triggered Si–O bond cleavage process in the fluoride-sensing mechanism of **TBS-NA**, the profile of free energy in solution was computed for the desilylation process (see Fig. 2). The formation of the intermediate, a complex between **TBS-NA** and F^-, is endergonic by 4.0 kcal/mol. In the intermediate complex, the fluoride anion interacts with **TBS-NA** through hydrogen-bond interaction [30, 31], and it has almost no interaction with silicon atom. A transition state ($\Delta G = 14.9$ kcal/mol) was located for the Si–O bond cleavage and F–Si bond formation. Relaxation of the transition state toward the intermediate and the products by IRC calculations did not detect any intermediates. Thus, the results indicated that the present desilylation reaction belonged to the S_N2 reaction type and had a low reaction barrier ($\Delta G = 14.9$ kcal/mol) for the Si–O bond cleavage and the formation of **NA** and **$SiCH_3F$**. Meanwhile, this low-barrier reaction induces the rapid response speed of the chemosensor **TBS-NA** for fluoride anion [27].

3.2 ^{1}H NMR spectra

Figure 3 shows the ^{1}H NMR spectra of **TBS-NA** and **NA**, calculated by using the B3LYP/QZVP method (tetramethylsilane was chosen as a standard substance in this calculation). For **TBS-NA**, the calculated signals at $\delta = 8.8$, 8.7, 8.6, 7.7 and 7.0 ppm are assigned to the protons of He, Hb, Hc, Hd and Ha, respectively. This calculation result agrees well with the previous experimental ^{1}H NMR spectrum (see Table S2) [27]. For the desilylation anion product **NA**, the calculated signals at $\delta = 8.7$, 8.4, 8.2, 7.2 and 6.2 ppm are assigned to the protons of the Hc′, He′, Hb′, Hd′ and Ha′, respectively. However, in the assignment of the measured ^{1}H NMR spectrum by Ren et al. [27], the three downfield signals that should be assigned to the three protons of Hc′, He′ and Hb′ have been wrongly assigned to Ha′, Hb′ and Hc′. In detail, the signals at $\delta = 6.5$ and 8.6 ppm have been both assigned to Ha′ in [27], but actually, the signal at

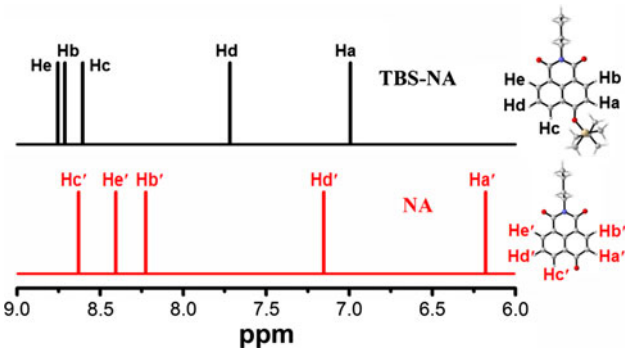

Fig. 3 Calculated ^{1}H NMR spectra of **TBS-NA** (up) and **NA** (down) at DFT/B3LYP/QZVP level, tetramethylsilane (TMS) is chosen as the standard substance

$\delta = 8.6$ ppm should be assigned to Hc′ instead of Ha′; the signals at $\delta = 8.4$ and 8.3 ppm should be assigned sequentially to He′ and Hb′ (see Table S3) instead of Hb′ and Hc′ in [27] (see Fig. 3). Comparison of the two spectra revealed that the proton signals of Ha′, Hb′, Hd′ and He′ shift to upfield while the proton signal of Hc′ shifts to downfield, which can be ascribed to the electron density redistribution of the π-conjugated framework as a result of the desilylation reaction.

3.3 Binding energy

We calculated the binding energies between the chemosensor **TBS-NA** and the basic anions to explain its high selectivity for the fluoride anion. For this aim, we first optimized the geometries of all the complexes formed between **TBS-NA** and the involved anions in [27]. And such optimizations were performed with DFT/B3LYP/TZVP and IEF–PCM (MeCN, $\varepsilon = 35.69$). Then, the binding energies were further derived from the formula: $E_{\text{binding}} = E_{\text{TBS-NA}} + E_{\text{Anion}} - E_{\text{Complex}}$. We note here that in this calculation the basis set superposition error (BSSE) has been accounted for using the counterpoise method of Boys and Bernardi [32]. Binding energies between **TBS-NA** and the anions in [27] (F^-, Cl^-, Br^-, I^-, ClO_4^-, AcO^-, HSO_4^-) are listed in Table 1. As seen, the binding energy between the fluoride anion and **TBS-NA** is more than two times larger than that between other anions and **TBS-NA**. The larger binding energies between fluoride anion and **TBS-NA** therefore induce **TBS-NA** having a high selectivity for the fluoride anion over other common anions [27]. On the other hand, one can also note that the anions such as Cl^- and Br^- can interact with **TBS-NA** and form the complex through weak binding. However, in the experiment, even when 10 equivalent of these ions (Cl^-, Br^-, I^-, ClO_4^-, AcO^-, HSO_4^-) was added, the absorbance spectrum of **TBS-NA** has merely displayed a small change [27]. Judged by this phenomenon, it is very likely that the complexes formed with these anions (Cl^-, Br^-, I^-, ClO_4^-, AcO^-, HSO_4^-) are not stable. In contrast, the added F^- can interact with **TBS-NA** to form a relatively stable complex through a larger binding energy of 28.8 kcal mol^{-1}. Therefore, we conjectured that the possibility is sparse for these anions of Cl^-, Br^-, I^-, ClO_4^-, AcO^-, HSO_4^- to compete with F^- in the binding process with **TBS-NA,** even at a quite high concentration (10 equivalent) [27].

Table 1 Calculated binding energies for **TBS-NA** with the anions involved in [27] using the B3LYP/TZVP method

Anions	Binding energies/kcal mol^{-1}
F^-	28.8
Cl^-	12.1
Br^-	11.7
I^-	4.5[a]
ClO_4^-	8.1
AcO^-	9.7
HSO_4^-	2.5

[a] Considering that iodine is out of range of the TZVP basis set, we choose QZVP basis set in the binding energy calculation between iodine anion and **TBS-NA**

3.4 UV–Vis absorption spectra and molecular orbital analysis

Based on the optimized geometries, the electronic transition energies and the corresponding oscillator strengths have been calculated for **TBS-NA** and **NA** using the TD-DFT/B3LYP/TZVP. For a reasonable comparison with the experimental spectra [27], our theoretical calculations predicted six low-lying absorbing transitions corresponding to the electronic transition energy ≤4.5 eV. Here, 4.5 eV is an upper energy limit value of the measured UV–Vis spectra of the **TBS-NA** system. Then, using the Gaussian models (see SI), the absorption profiles were calculated and compared with the experimental measurements. As shown in Fig. 4, our calculated results agree well with the experimental spectra. The figure also shows that with the addition of the fluoride anion, a large observable redshift was seen, that is, the peak at 362 nm disappeared and the redshift band at 474 nm appeared [27]. Tables 2, S4 and S5 list the calculated electronic transition energies and the corresponding oscillator strengths (*f*) of the singlet excited states for **TBS-NA** and **NA**, together with the experimental results of absorbance titration. The first singlet transition ($S_0 \rightarrow S_1$) of **TBS-NA** is theoretically predicted to be located at 377 nm, thus well reproduced the experimental result where the absorbance band of **TBS-NA** is located at 362 nm [27]. For the desilylation product **NA**, the

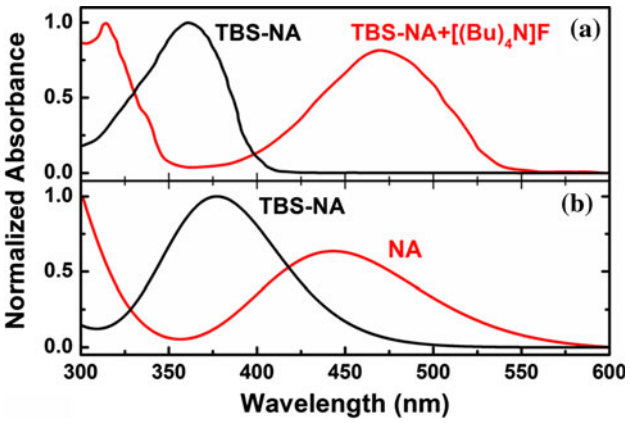

Fig. 4 Comparison of experimental and calculated UV–Vis absorption spectra. **a** Experimental UV–Vis spectra of **TBS-NA** in MeCN with the addition of 1 equivalent $[(Bu)_4N]F$ (taken from [27]); **b** the calculated absorption bands of **TBS-NA** and **NA** obtained at the TD-DFT/B3LYP/TZVP level

calculated first singlet transition ($S_0 \rightarrow S_1$) located at 443 nm agrees well with the absorbance band located at 474 nm of **TBS-NA** with the addition of 1 equivalent $[(Bu)_4N]F$ [27]. Hence, such large observable redshift between the spectra of **TBS-NA** and its desilylation product **NA** is essential for **TBS-NA** to be served as a ratiometric chemosensor for fluoride anion.

In order to explain the large observable redshift of **TBS-NA** with the addition of the 1 equivalent $[(Bu)_4N]F$, we calculated the frontier molecular orbitals for **TBS-NA** and **NA,** which are shown in Fig. 5. From Table 2, we can see that the CI value, which represents the contribution of the ground-state orbitals to the ground- to first-excited-state transition, is less than 1, thus indicating an inadequacy of using the ground-state frontier molecular orbitals to describe the electronic state transition. However, in the present case the CI values of 0.97 are approaching to 1, which supports that the first singlet transition ($S_0 \rightarrow S_1$) in the **TBS-NA** system can be mostly described as HOMO → LUMO using the ground-state orbitals. Based on this and in order to compare the charge separation character between **TBS-NA** and **NA**, we divided **TBS-NA** and **NA** into two parts (see Fig. S1 for part 1 and part 2) and calculated the contributions of part 1 and part 2 to frontier molecular orbitals by C-squared population analysis [33] method. The corresponding results are listed in Table S6. For HOMO of **TBS-NA**, there is 40 % of the electron density residing on the part 1 and 60 % on part 2, while for LUMO of **TBS-NA**, 29 % of the electron density resides on part 1 and 71 % on part 2. In the case of **NA** and for HOMO, there is 52 % of the electron density residing on part 1 and 48 % on part 2, while for LUMO, there is 19 % of the electron density residing on part 1 and 81 % on part 2. From these results, one can note that the first excited state S_1 of **NA** possesses relatively more charge separation character [34], and this relatively ICT process can lead to the redshift in the absorption spectrum of the desilylation product **NA**, as compared with that of **TBS-NA** [7].

3.5 First-excited-state geometries and sensing mechanism

From the viewpoint of analytical science, a dye's light emission is much more sensitive than its light absorption [35]. As previously reported, the chemosensors based on 4-amino-1,8-naphthalimides are usually typical fluorophores with an ICT character [35], and most of them can be a good candidate for fluorescent chemosensor [1, 35]. Hence, in this section, we shall investigate the emission characters of the chemosensor **TBS-NA** to verify its potential as a fluorescent chemosensor for fluoride anion. In order to do this, we studied the first excited state (S_1) of **TBS-NA** and **NA** using the TD-DFT/B3LYP/TZVP method. The optimized first-excited-state structures of

Table 2 Comparison of experimental and the calculated absorbance band at TD-DFT/B3LYP/TZVP level

		TBS-NA	**NA**
Theoretical data	Electronic transition[a]	$S_0 \rightarrow S_1$	$S_0 \rightarrow S_1$
	Energy (nm/eV)	377 (3.29)	443 (2.80)
	f[b]	0.3445	0.1970
	Contribution[c]	HOMO → LUMO	HOMO → LUMO
	CI[d]	0.97	0.97
Experimental data	Absorbance band (nm)[e]	362	474

[a] Only the first-excited-state transition is presented here, and all other calculated excitations are presented in Tables S4 and S5

[b] Oscillator strength

[c] Only the main configurations are presented

[d] The CI coefficients are in absolute values

[e] The experimental absorbance band taken from [27]

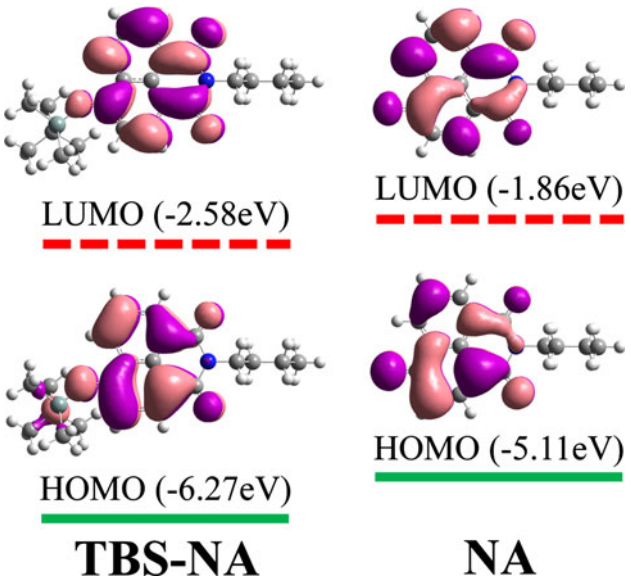

Fig. 5 Calculated frontier molecular orbitals HOMO and LUMO for **TBS-NA**, HOMO and LUMO for **NA**

TBS-NA and **NA** are displayed in Fig. S2, and the atomic coordinates of these structures are provided in the Supporting Information. From these calculation results, we can see that in the first excited state, **TBS-NA/NA** shares the similar structure with that in the ground state. The calculated $S_1 \rightarrow S_0$ vertical excitation energies are located at 443 and 540 nm, respectively, for **TBS-NA** and **NA**. Compared with **TBS-NA,** the calculated fluorescence emission spectrum of **NA** has a redshift of $\sim$100 nm, as shown in Fig. S3. The redshift emission spectrum of **NA** is again ascribed to its relatively strong ICT character. Because of the redshift character of the fluorescence emission spectra, the chemosensor **TBS-NA** can serve as a fluorescent chemosensor for fluoride anion.

Finally, we can understand the sensing mechanism of **TBS-NA** to be based on these steps: The added fluoride anion triggered the Si–O bond cleavage reaction in **TBS-NA** and formed the two products of **NA** and **$SiCH_3F$**. Since the first excited state of the desilylation product **NA** possesses relatively strong ICT, both the emission and the absorption spectra of **NA** exhibit a large observable redshift and thus guarantee that **TBS-NA** can serve as a colorimetric chemosensor for fluoride anion.

4 Conclusion

By applying DFT/TD-DFT methods, we have investigated the fluoride-sensing mechanism of chemosensor **TBS-NA**. The fluoride anion triggered Si–O cleavage reaction, where the Si–O bond of **TBS-NA** is cleaved by the added fluoride anion and the two products of **NA** and **$SiCH_3F$** are formed, laid a basis for the sensing properties of **TBS-NA**. This reactive process has been further verified to be low barrier from the calculated profile of free energy in solution of **TBS-NA**. The optimized structures for **TBS-NA** and **NA** in both the ground and the excited states and for the fluoride complex form **TBS-NAF** in the ground state, the ^{1}H NMR spectra and the UV–Vis spectra for **TBS-NA** and **NA** have also been obtained. The experimental UV–Vis absorbance spectra are well reproduced by the calculated vertical excitation energies. Because of the relatively strong ICT process of $S_0 \rightarrow S_1$ transition in **NA**, the absorbance spectrum of **NA** exhibits the redshift as compared with that of **TBS-NA**. The ICT process leads to the redshift of the calculated fluorescence emission spectrum of **NA** as well. The large observable redshift supported that the chemosensor **TBS-NA** has the potential as a fluorescent chemosensor for fluoride anion. Moreover, we have corrected the wrongly assigned experimental ^{1}H NMR in the present study.

References

1. Du JJ, Hu MM, Fan JL, Peng XJ (2012) Fluorescent chemodosimeters using "mild" chemical events for the detection of small anions and cations in biological and environmental media. Chem Soc Rev 41:4511–4535
2. Cheng XH, Li S, Xu GH, Li CG, Qin JG, Li Z (2012) A reaction-based colorimetric fluoride probe: rapid "Naked-Eye" detection and large absorption shift. ChemPlusChem 77:908–913
3. Zhu BC, Yuan F, Li RX, Li YM, Wei Q, Ma ZM, Du B, Zhang XL (2011) A highly selective colorimetric and ratiometric fluorescent chemodosimeter for imaging fluoride ions in living cells. Chem Commun 47:7098–7100
4. Sun HB, Dong XC, Liu SJ, Zhao Q, Mou X, Yang HY, Huang W (2011) Excellent BODIPY Dye Containing Dimesitylboryl groups as PeT-based fluorescent probes for fluoride. J Phys Chem C 115:19947–19954
5. Bozdemir OA, Sozmen F, Buyukcakir O, Guliyev R, Cakmak Y, Akkaya EU (2010) Reaction-based sensing of fluoride ions using built-in triggers for intramolecular charge transfer and photoinduced electron transfer. Org Lett 12:1400–1403
6. Gai LZ, Chen HC, Zou B, Lu H, Lai GQ, Li ZF, Shen Z (2012) Ratiometric fluorescence chemodosimeters for fluoride anion based on pyrene excimer/monomer transformation. Chem Commun 48:10721–10723
7. Wu J, Liu W, Ge J, Zhang H, Wang P (2011) New sensing mechanisms for design of fluorescent chemosensors emerging in recent years. Chem Soc Rev 40:3483–3495
8. Jagtap S, Yenkie MK, Labhsetwar N, Rayalus S (2012) Fluoride in drinking water and defluoridation of water. Chem Rev 112:2454–2466
9. Kumar JV, Moss ME (2008) Fluorides in dental public health programs. Dent Clin North Am 5:387–401
10. Singh PP, Barjatiya MK, Dhing S, Bhatnagar R, Kothari S, Dhar V (2001) Evidence suggesting that high intake of fluoride provokes nephrolithiasis in tribal populations. Urol Res 29:238–244
11. Kurishita Y, Kohira T, Ojida A, Hamachi I (2010) Rational design of FRET-based ratiometric chemosensors for in vitro and

in cell fluorescence analyses of nucleoside polyphosphates. J Am Chem Soc 132:13290–13299
12. Mashraqui SH, Ghorpade SS, Tripathi S, Britto S (2012) A new indole incorporated chemosensor exhibiting selective colorimetric and fluorescence ratiometric signaling of fluoride. Tetrahedron Lett 53:765–768
13. Peng XJ, Wu YK, Fan JL, Tian MZ, Han KL (2005) Colorimetric and ratiometric fluorescence sensing of fluoride: tuning selectivity in proton transfer. J Org Chem 70:10524–10531
14. Luxami V, Kumar S (2007) Colorimetric and ratiometric fluorescence sensing of fluoride ions based on competitive intra- and intermolecular proton transfer. Tetrahedron Lett 48:3083–3087
15. Chen ZJ, Wang LM, Zou G, Zhang L, Zhang GJ, Cai XF, Teng MS (2012) Colorimetric and ratiometric fluorescent chemosensor for fluoride ion based on perylene diimide derivatives. Dyes Pigm 94:410–415
16. Mallick A, Roy UK, Haldar B, Pratihar S (2012) A newly developed highly selective ratiometric fluoride ion sensor: spectroscopic, NMR and density functional studies. Analyst 137:1247–1251
17. Zheng F, Zeng F, Yu C, Hou X, Wu S (2013) A PEGylated fluorescent turn-on sensor for detecting fluoride ions in totally aqueous media and its imaging in live cells. Chem Eur J 19:936–942
18. Bao YY, Liu B, Wang H, Tian J, Bai RK (2011) A "naked eye'' and ratiometric fluorescent chemosensor for rapid detection of F(-) based on combination of desilylation reaction and excited-state proton transfer. Chem Commun 47:3957–3959
19. Dong M, Peng Y, Dong YM, Tang N, Wang YW (2012) A selective, colorimetric, and fluorescent chemodosimeter for relay recognition of fluoride and cyanide anions based on 1,1′-Binaphthyl Scaffold. Org Lett 14:130–133
20. Yang XF, Qi HP, Wang LP, Su Z, Wang G (2009) A ratiometric fluorescent probe for fluoride ion employing the excited-state intramolecular proton transfer. Talanta 80:92–97
21. Li GY, Chu TS (2011) TD-DFT study on fluoride-sensing mechanism of 2-(2′-phenylureaphenyl)benzoxazole: the way to inhibit the ESIPT process. Phys Chem Chem Phys 13:20766–20771
22. Li GY, Zhao GJ, Liu YH, Han KL, He GZ (2010) TD-DFT study on the sensing mechanism of a fluorescent chemosensor for fluoride: excited-state proton transfer. J Comput Chem 31:1759–1765
23. Xu WJ, Liu SJ, Zhao XY, Sun S, Cheng S, Ma TC, Sun HB, Zhao QA, Huang W (2010) Cationic Iridium(III) complex containing both Triarylboron and carbazole moieties as a ratiometric fluoride probe that utilizes a switchable triplet-singlet emission. Chem Eur J 16:7125–7133
24. Li GY, Li YH, Zhang H, Cui GH (2013) Time-dependent density functional theory study on a fluorescent chemosensor based on C–H…F hydrogen-bond interaction. Commun Comput Chem 1:88–98
25. Chen JS, Zhou PW, Li GY, Chu TS, He GZ (2013) Fluoride anion sensing mechanism of 2-ureido-4[1H]-pyrimidinone quadruple hydrogen-bonded supramolecular assembly: photoinduced electron transfer and partial configuration change. J Phys Chem B 117:5212–5221
26. Jin R, Zhang J (2009) Theoretical investigation of chemosensor for fluoride anion based on amidophthalimide derivatives. Theor Chem Acc 124:225–234
27. Ren J, Wu Z, Zhou Y, Li Y, Xu Z (2011) Colorimetric fluoride sensor based on 1,8-naphthalimide derivatives. Dyes Pigm 91:442–445
28. Frisch MJ, Trucks GW, Schlegel HB, Scuseria GE, Robb MA, Cheeseman JR, Scalmani G, Barone V, Mennucci B, Petersson GA, Nakatsuji H, Caricato M, Li X, Hratchian HP, Izmaylov AF, Bloino J, Zheng G, Sonnenberg JL, Hada M, Ehara M, Toyota K, Fukuda R, Hasegawa J, Ishida M, Nakajima T, Honda Y, Kitao O, Nakai H, Vreven T, Montgomery JA, Jr., Peralta JE, Ogliaro F, Bearpark M, Heyd JJ, Brothers E, Kudin KN, Staroverov VN, Keith T, Kobayashi R, Normand J, Raghavachari K, Rendell A, Burant JC, Iyengar SS, Tomasi J, Cossi M, Rega N, Millam JM, Klene M, Knox JE, Cross JB, Bakken V, Adamo C, Jaramillo J, Gomperts R, Stratmann RE, Yazyev O, Austin AJ, Cammi R, Pomelli C, Ochterski JW, Martin RL, Morokuma K, Zakrzewski VG, Voth GA, Salvador P, Dannenberg JJ, Dapprich S, Daniels AD, Farkas O, Foresman JB, Ortiz JV, Cioslowski J, Fox DJ (2010) Gaussian, Inc., Wallingford CT
29. Nikolin AA, Kramarova EP, Shipov AG, Baukov YI, Negrebetsky VV, Korlyukov AA, Arkhipov DE, Bowden A, Bylikin SY, Bassindale AR, Taylor PG (2012) Synthesis, structures, and stereodynamic behavior of novel pentacoordinate fluorosilanes: fluorosilyl derivatives of proline. Organometallics 31:4988–4997
30. Zhao GJ, Han KL (2012) Hydrogen bonding in the electronic excited state. Acc Chem Res 45:404–413
31. Han KL, Huang JD, Chai S, Wen SH, Deng WQ (2013) Anisotropic mobilities in organic semiconductors. Protocol Exchange. doi:10.1038/protex.2013.070
32. Boys SF, Bernardi F (2002) The calculation of small molecular interactions by the differences of separate total energies. Some procedures with reduced errors. Mol Phys 100:65–73
33. Ros P, Schuit GCA (1966) Molecular orbital calculations on copper chloride complexes. Theor Chim Acta 4:1–12
34. Pollock JB, Cook TR, Stang PJ (2012) Photophysical and computational investigations of Bis(phosphine) Organoplatinum(II) Metallacycles. J Am Chem Soc 134:10607–10620
35. Qian X, Xiao Y, Xu Y, Guo X, Qian J, Zhu W (2010) "Alive" dyes as fluorescent sensors: fluorophore, mechanism, receptor and images in living cells. Chem Commun 46:6418–6436